

Anomalous Hall effect and Lifshitz transition in Fe_3Sn_2 nanosheets

Xue Yang(杨雪), Jijian Liu(刘继健), Xinyi Zheng(郑新义), Lei Xu(徐磊), Lihong Hu(胡利洪), Sicheng Zhou(周思成), Siyuan Zhou(周思远), Ximing Zhang(张栖铭), Bingbing Tong(仝冰冰), Jie Shen(沈洁), Zhaozheng Lyu(吕昭征), Xiunian Jing(景秀年), Fanming Qu(屈凡明), Peiling Li(李沛岭), Jiadong Zhou(周家东), Guangtong Liu(刘广同), and Li Lü(吕力)

Citation: Chin. Phys. B, 2026, 35 (**1**): 017503. DOI: 10.1088/1674-1056/ae101b
http://cpb.iphy.ac.cn; http://iopscience.iop.org/cpb

What follows is a list of articles you may be interested in

Tunable anomalous Hall effect and anisotropic magnetism in In-doped $TbMn_6Sn_6$ kagome magnets

Detong Wu(吴德桐), Jianwei Qin(秦建伟), and Bing Shen(沈冰)
Chin. Phys. B, 2025, 34 (**10**): 107511. DOI: 10.1088/1674-1056/adde37

Evolution of anomalous Hall effect in ferromagnetic Weyl semimetal $Nb_xZr_{1-x}Co_2Sn$

Bo-Wen Chen(陈博文) and Bing Shen(沈冰)
Chin. Phys. B, 2024, 33 (**8**): 087501. DOI: 10.1088/1674-1056/ad4a3b

Tailoring-compensated ferrimagnetic state and anomalous Hall effect in quaternary Mn-Ru-V-Ga Heusler compounds

Jin-Jing Liang(梁瑾静), Xue-Kui Xi(郗学奎), Wen-Hong Wang(王文洪), and Yong-Chang Lau(刘永昌)
Chin. Phys. B, 2024, 33 (**7**): 077504. DOI: 10.1088/1674-1056/ad34c8

Enhanced anomalous Hall effect in kagome magnet $YbMn_6Sn_6$ with intermediate-valence ytterbium

Longfei Li(李龙飞), Shengwei Chi(迟晟玮), Wenlong Ma(马文龙), Kaizhen Guo(郭凯臻), Gang Xu(徐刚), and Shuang Jia(贾爽)
Chin. Phys. B, 2024, 33 (**5**): 057501. DOI: 10.1088/1674-1056/ad322d

Angular and planar transport properties of antiferromagnetic V_5S_8

Xiao-Kai Wu(吴晓凯), Bin Wang(王彬), De-Tong Wu(吴德桐), Bo-Wen Chen(陈博文), Meng-Juan Mi(弭孟娟), Yi-Lin Wang(王以林), and Bing Shen(沈冰)
Chin. Phys. B, 2024, 33 (**2**): 027503. DOI: 10.1088/1674-1056/ad15f9

RAPID COMMUNICATION

Anomalous Hall effect and Lifshitz transition in Fe_3Sn_2 nanosheets

Xue Yang(杨雪)[1,2,†], Jijian Liu(刘继健)[3,4,†], Xinyi Zheng(郑新义)[1,2], Lei Xu(徐磊)[1,2], Lihong Hu(胡利洪)[1,2], Sicheng Zhou(周思成)[1,2], Siyuan Zhou(周思远)[1,2], Ximing Zhang(张栖铭)[1,2], Bingbing Tong(仝冰冰)[1,5], Jie Shen(沈洁)[1,2,5], Zhaozheng Lyu(吕昭征)[1,2], Xiunian Jing(景秀年)[1], Fanming Qu(屈凡明)[1,2,5], Peiling Li(李沛岭)[1,2,5,‡], Jiadong Zhou(周家东)[3,4,§], Guangtong Liu(刘广同)[1,2,5,¶], and Li Lü(吕力)[1,2,5]

[1] *Institute of Physics and Beijing National Laboratory for Condensed Matter Physics, Chinese Academy of Sciences, Beijing* 100190, *China*
[2] *School of Physical Sciences, University of Chinese Academy of Sciences, Beijing* 100049, *China*
[3] *Centre for Quantum Physics, Key Laboratory of Advanced Optoelectronic Quantum Architecture and Measurement (MOE), Beijing Institute of Technology, Beijing* 100081, *China*
[4] *School of Physics, Beijing Institute of Technology, Beijing* 100081, *China*
[5] *Hefei National Laboratory, Hefei* 230088, *China*

(Received 1 August 2025; revised manuscript received 30 September 2025; accepted manuscript online 7 October 2025)

Fe_3Sn_2, a ferromagnetic metal with a kagome lattice, serves as an ideal platform for exploring topological electronic states and Berry curvature due to its unique band structure. However, systematic reports on the transport properties of Fe_3Sn_2 nanosheets remain scarce. We present temperature-dependent transport property measurements of Fe_3Sn_2 nanosheets synthesized via chemical vapor deposition on Si/SiO_2 substrates. The samples exhibit a robust anomalous Hall effect from 40 K to 300 K, along with a magnetoresistance sign reversal at 40 K at high magnetic fields, indicating a spin reorientation from in-plane to out-of-plane. Notably, a sharp crossover in the dominant transport contribution from electrons to holes near 200 K is observed, accompanied by distinct anomalous Hall behaviors in the two regimes, indicating a temperature-induced Lifshitz transition within the multi-band system. This divergence is potentially linked to a topological reconstruction of the Fermi surface across the transition. Our findings highlight the tunability of topological transport in two-dimensional kagome magnets and provide new insights into the interplay between band topology, dimensionality and magnetic order.

Keywords: kagome materials, anomalous Hall effect, ferromagnetism, Lifshitz transition

PACS: 75.50.Cc, 73.43.Qt, 87.15.Zg

DOI: 10.1088/1674-1056/ae101b **CSTR:** 32038.14.CPB.ae101b

1. Introduction

The kagome lattice, characterized by its corner-sharing triangular geometry, has emerged as a prototypical platform for investigating geometrical frustration and topological quantum states.[1,2] Its unique band structure — featuring Dirac nodes, flat bands, and van Hove singularities[3,4] — intertwines with magnetic order to give rise to emergent phenomena, notably the Berry-curvature driven anomalous Hall effect (AHE).[5–7] When the Fermi level approaches these singularities, even modest perturbations such as temperature variation, external magnetic fields, or carrier doping can induce a Lifshitz transition (a topological reconstruction of the Fermi surface),[8–11] resulting in abrupt changes in transport and magnetic properties. Temperature-driven Lifshitz transitions have been observed in kagome materials including $Mn_{3.1-x}Fe_xGe_{0.9}$,[12] Mn_3Ge,[13] $LiMn_6Sn_6$,[14] and Nd_3Al.[15] These discoveries demonstrate the tunability of Berry curvature in kagome systems and broaden their prospects for applications in topological spintronics.

Among magnetic kagome metals, Fe_3Sn_2 is particularly notable for its high Curie temperature ($T_C \approx 650$ K) and strong electronic correlations.[16–18] Angle-resolved photoemission spectroscopy (ARPES) has confirmed the presence of massive Dirac fermions and a flat band near the Fermi level in bulk samples.[19] It exhibits a robust AHE persisting up to room temperature, alongside a spin reorientation transition around 80 K.[20,21] Above 100 K, a characteristic hump in the Hall signal suggests the presence of a topological Hall effect (THE) associated with non-collinear spin textures,[22,23] supported by Lorentz transmission electron microscopy (LTEM) observations of skyrmionic bubbles in a similar temperature range.[24–26] While most previous studies have focused on bulk crystals or films synthesized via chemical vapor transport (CVT)[22,27] or molecular beam epitaxy (MBE)[28,29] methods, only a single report by Zhu *et al.* has investigated chemical vapor deposition (CVD)-grown Fe_3Sn_2 nanosheets ($\sim$ 10–20 nm) and their transport behavior.[30] Notably, the temperature-driven Lifshitz transition remains largely unex-

[†]These authors contributed equally to this work.
[‡]Corresponding author. E-mail: cioran@iphy.ac.cn
[§]Corresponding author. E-mail: jdzhou@bit.edu.cn
[¶]Corresponding author. E-mail: gtliu@iphy.ac.cn

© 2026 Chinese Physical Society and IOP Publishing Ltd. All rights, including for text and data mining, AI training, and similar technologies, are reserved.

plored in this two-dimensional limit, despite its potential impact on the electronic structure and topological transport in reduced dimensions.

In this work, we systematically report the temperature-dependent transport properties of Fe_3Sn_2 nanosheets synthesized via CVD on Si/SiO_2 substrates. The AHE emerges above 40 K and persists up to room temperature, while the magnetoresistance undergoes a transition from positive to negative at high fields around 40 K, suggesting a reorientation of magnetic moments from in-plane to out-of-plane, consistent with prior observations in bulk Fe_3Sn_2. Furthermore, a clear switch in the dominant charge carrier from electrons to holes is observed near 200 K, signifying a temperature-driven Lifshitz transition within the multi-band system. Through scaling analysis, we identify that both skew scattering and intrinsic Berry curvature contribute to the AHE and reveal contrasting anomalous Hall behaviors across the transition. This divergence further supports the presence of a Lifshitz transition and possibly originates from the underlying reconstruction of the Fermi surface topology. These findings establish a foundation for further exploration of topological phase transitions and anomalous transport in low-dimensional kagome systems.

2. Experimental details

The Fe_3Sn_2 nanosheets were synthesized via CVD method. Stoichiometric amounts of Fe and Sn were sealed in an evacuated quartz tube, with a silicon substrate placed in the deposition zone. The elemental composition was verified by energy-dispersive x-ray spectroscopy (EDS), and the thickness of nanosheets was determined with atomic force microscopy (AFM). Multiple Hall-bar devices were fabricated using electron-beam lithography (EBL) followed by Ti/Au (5/60 nm) electrode deposition. Electrical transport measurements were performed in a Quantum Design physical property measurement system (PPMS) at temperatures ranging from 2 K to 300 K and magnetic fields up to 9 T.

3. Results and discussion

Fe_3Sn_2 is a centrosymmetric magnet belonging to the space group $R\bar{3}m$. Its crystal structure consists of an alternating stack of Fe–Sn bilayers and Sn honeycomb layers, as illustrated in Fig. 1(a). Each Fe–Sn bilayer features a Fe-based kagome lattice with a central Sn atom located at the center of the hexagon. In the Sn honeycomb layer, all Sn atoms occupy the honeycomb lattice sites. EDS analysis (Fig. 1(b)) yields an Fe:Sn atomic ratio of 1.43:1 for the hexagonal Fe_3Sn_2 sample. The slight deviation from the ideal stoichiometric ratio of 1.5:1 may be attributed to Fe deficiency, which can regulate Fe_3Sn_2 sample morphology and the coercivity of AHE, in line with previous observations.[30] AFM results (Fig. 1(c)) reveal that the Fe_3Sn_2 nanoflakes have a thickness of approximately 25 nm. Figure 1(d) shows the temperature dependence of the longitudinal resistivity (R_{xx}) measured with current (I) applied within the ab-plane. The monotonic decrease in R_{xx} upon cooling confirms a highly metallic ground state. Furthermore, the residual resistivity ratio (RRR $= R_{400\ \mathrm{K}}/R_{2\ \mathrm{K}}$) is 38.73, exceeding values reported for previous Fe_3Sn_2 samples.[23,30,31] Collectively, these characterization results demonstrate that the CVD-grown Fe_3Sn_2 nanosheets exhibit a well-defined morphology and significant electrical transport properties.

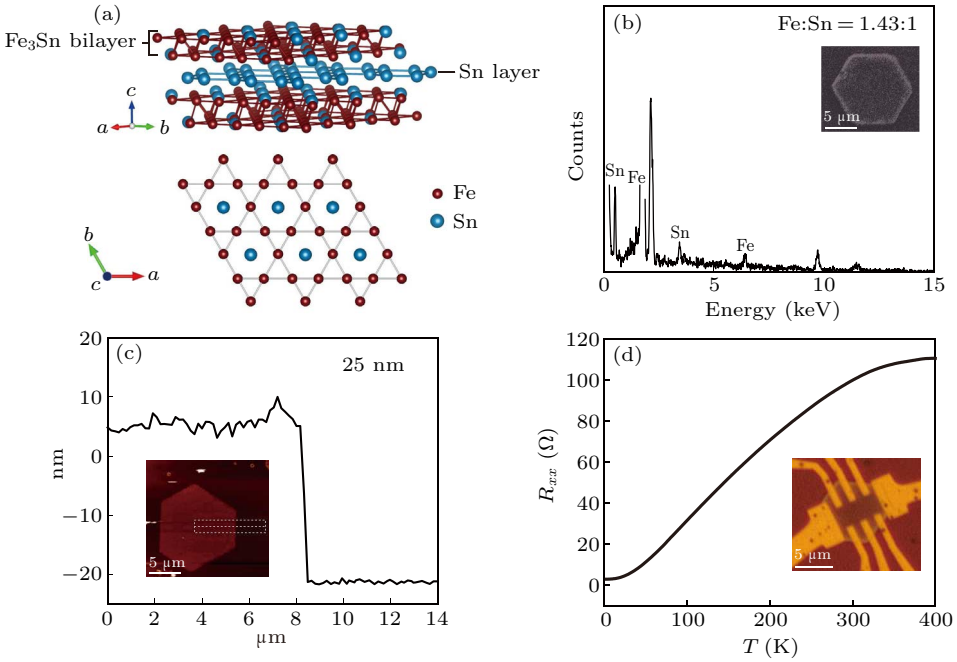


Fig. 1. (a) Crystal structure of Fe_3Sn_2, in which the Fe–Sn bilayers and Sn layers stack along the c-axis alternatively. The upper panel shows the side view of the Fe_3Sn_2 crystal, while the lower panel presents the top view of the Fe_3Sn layer, highlighting the kagome lattice. Brown and blue balls represent Fe and Sn atoms, respectively. (b) EDS spectrum of the hexagonal Fe_3Sn_2, which shows an Fe:Sn atomic ratio of 1.43:1, close to the ideal stoichiometric ratio of 1.5. The inset shows an image of a hexagonal Fe_3Sn_2 captured by scanning electron microscopy. (c) AFM mapping of Fe_3Sn_2 with a thickness of about 25 nm; the inset shows the tested Fe_3Sn_2 sample. (d) Temperature-dependent longitudinal resistance (R_{xx}) of Fe_3Sn_2.The device diagram is shown in the lower right inset.

Figure 2(a) presents the magnetoresistance (MR) measured with the magnetic field ($\mu_0 H$) applied perpendicular to sample plane (along the c-direction), swept from -3 T to 3 T at various temperatures. Our measurements reveal a parabolic positive MR persisting up to 40 K at high fields. Above this temperature, the high-field MR gradually turns negative, and a well-defined MR valley deepens with decreasing temperature at low fields, indicating a progressive spin reorientation transition. This transition reflects the rotation of the magnetic easy axis from the c-axis towards the ab-plane, eventually aligning in-plane below 80 K.[20] The low-field MR valley originates from incomplete spin alignment, where enhanced scattering from defects and magnons leads to positive MR.[32,33] As the field increases and spins align, spin-disorder and orbital scattering are suppressed, resulting in negative MR.[34,35] As the temperature rises, spin reorientation becomes more pronounced, gradually diminishing the MR valley. These characteristic features align with prior magnetoresistance studies,[36] highlighting the intrinsic properties that differentiate our thin film samples from the bulk materials.

The Hall resistivity (ρ_{xy}) of Fe_3Sn_2 nanosheets measured from 2 K to 300 K is displayed in Fig. 2(b). At high magnetic fields, ρ_{xy} exhibits a linear dependence on $\mu_0 H$, attributed to the ordinary Hall effect. Below 20 K, the Hall resistivity remains linear with a negative slope, indicating that electron carriers dominate the transport. As the temperature increases, a noticeable deviation from linearity emerges at low fields, particularly above 40 K, signifying the onset of a pronounced AHE. Importantly, the magnetic field at which ρ_{xy} saturates coincides with the point where the MR curve transitions from a low-field valley to negative magnetoresistance, further suggesting that this MR transition is governed by the spin alignment associated with the AHE. As the temperature rises further to approximately 200 K, the sign of the high-field slope of ρ_{xy} reverses from negative to positive, indicating a shift in the dominant carrier type from electrons to holes. This phenomenon has not been specifically observed and studied in the bulk/film Fe_3Sn_2.

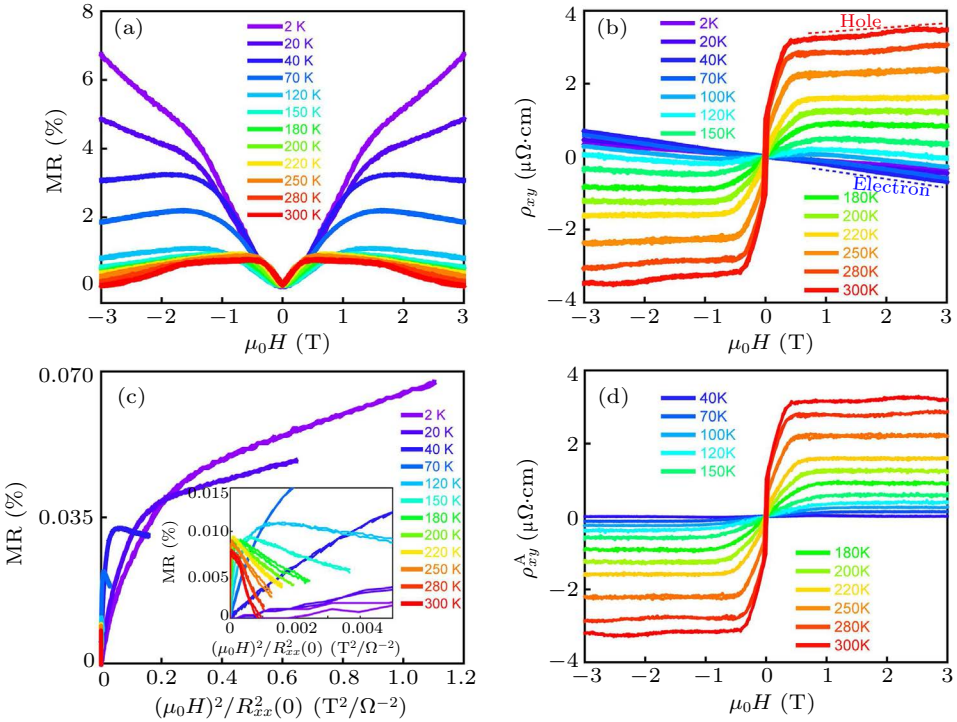


Fig. 2. (a) Magnetoresistance ($\mathrm{MR} = [\rho_{xx}(H) - \rho_{xx}(0\,\mathrm{T})]/\rho_{xx}(0\,\mathrm{T})$) measured under an out-of-plane field from 2 K to 300 K. (b) Hall resistivity (ρ_{xy}) as a function of the magnetic field across the same temperature range. (c) Kohler's rule for the magnetoresistance (MR). The MR data are replotted as MR versus $(\mu_0 H)^2/R_{xx}^2(0)$. (d) Extracted anomalous Hall resistivity (ρ_{xy}^{A}) from 40 K to 300 K, obtained by subtracting the linear ordinary Hall background.

The total Hall resistivity ρ_{xy} can be decomposed into ordinary ($\rho_{xy}^{\mathrm{O}}(H)$) and anomalous ($\rho_{xy}^{\mathrm{A}}(H)$) components as follows:

$$\rho_{xy}(H) = \rho_{xy}^{\mathrm{O}}(H) + \rho_{xy}^{\mathrm{A}}(H) = R_0 H + \rho_{xy}^{\mathrm{A}}(H), \qquad (1)$$

where R_0 is the ordinary Hall coefficient and ρ_{xy}^{A} represents the anomalous Hall resistivity. To elucidate the origin of the high-field Hall slope reversal, we consider two possible mechanisms: a multiband scattering effect or a Lifshitz transition involving Fermi surface reconstruction. To distinguish between these scenarios, we examined Kohler's rule, which predicts a unified scaling of MR curves when a single carrier type with constant scattering dominates.[37] As shown in Fig. 2(c), the MR curves at different temperatures deviate significantly from Kohler's rule. The invalidity is frequently associated with alterations in the Fermi surface and structure.[38]

To decouple the contributions from different carriers in the complex Fermi surface of Fe_3Sn_2, we consider the multi-band Drude model, the conductance component of each band can be expressed as

$$\sigma_{xx}^{i}(H) = \frac{n_i e \mu_i}{1+(\mu_i \mu_0 H)^2},$$
$$\sigma_{xy}^{i}(H) = \frac{s_i n_i e \mu_i^2 \mu_0 H}{1+(\mu_i \mu_0 H)^2}. \quad (2)$$

The total conductance is

$$\sigma_{xx}(H) = \sum_i \sigma_{xx}^{i}(H) = \sum_i \frac{n_i e \mu_i}{1+(\mu_i \mu_0 H)^2}, \quad (3)$$

$$\sigma_{xy}(H) = \sum_i \sigma_{xy}^{i}(H) = \sum_i \frac{s_i n_i e \mu_i^2 \mu_0 H}{1+(\mu_i \mu_0 H)^2}, \quad (4)$$

where n_i and μ_i are the carrier concentrations and mobilities, $s_i = 1$ for holes and $s_i = -1$ for electrons, and to eliminate the influence of anomalous Hall effect, the fitting is restricted in the region beyond the saturated magnetic field. With the mobility in Fe_3Sn_2 much lower than 10^4 $cm^2/V{\cdot}s$,[19,30] the low-field approximation ($\mu_i \mu_0 H \ll 1$) is satisfied, and the Hall coefficient is approximated as $R_0 \approx \frac{1}{e} \cdot \frac{\sum_i s_i n_i \mu_i^2}{(\sum_i n_i \mu_i)^2}$. Therefore, the slope of the linear ordinary Hall effect at high magnetic field depends on the weighted carrier concentration ($s_i n_i \mu_i^2$). After subtracting this linear ordinary background, the anomalous Hall resistivity ρ_{xy}^{A} is obtained, as shown in Fig. 2(d).

Furthermore, the sign of R_0 directly reflects the dominant carrier type: $R_0 > 0$ (i.e., $n_h \mu_h^2 > n_e \mu_e^2$) corresponds to hole-dominated transport, while $R_0 < 0$ ($n_h \mu_h^2 < n_e \mu_e^2$) corresponds to electron-dominated transport. As plotted in Fig. 3(a), R_0 remains negative below 200 K, consistent with electron-dominated behavior. As the temperature rises above 200 K, R_0 reverses sign. Supported by DFT and ARPES studies confirming that the Fermi level lies near topological flat bands and mixed electron–hole pockets,[39–41] we attribute the observed transport behavior primarily to a Lifshitz transition.[42,43] Such a transition involves a reconstruction of the Fermi surface, likely including the emergence of new hole pockets, which can simultaneously account for the carrier-type reversal and the concomitant changes in the scattering behavior. The reversal of R_0 provides a clear evidence of the temperature-driven Lifshitz transition likely associated with a continuous evolution of the Fermi surface topology.[44]

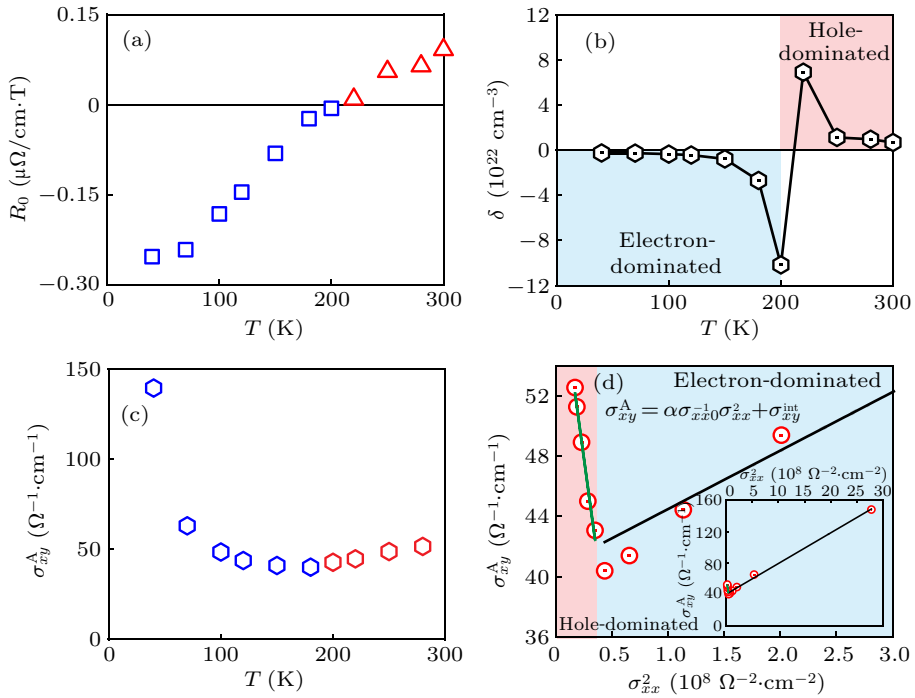


Fig. 3. (a) Temperature dependence of the ordinary Hall coefficient R_0 extracted from the high-field linear component of ρ_{xy}. The blue circle represents the R_0 below 200 K, which are negative, while the red triangle represents the R_0 from 220 K–300 K, which are positive. (b) Weighted carrier concentration δ (black hexagon) as a function of temperature, derived from the extracted R_0 values. (c) Temperature dependence of the anomalous Hall conductivity σ_{xy}^{A}. The blue hexagon represents the σ_{xy}^{A} below 200 K, and the red hexagon represents the σ_{xy}^{A} from 220 K–300 K. (d) An enlarged view of σ_{xy}^{A} in the low conductivity (high temperature) region. Inset: extracted σ_{xy}^{A} as a function of σ_{xx}^{2} from 40 K to 300 K. The solid black and green lines represent the fitting results for the high- and low-conductivity regimes, respectively, based on the scaling relation in Eq. (5). The red and blue shaded regions correspond to hole- and electron-dominated transport, respectively, with the data point at 200 K marking the crossover boundary.

Given $\delta = \frac{(\sum_i n_i \mu_i)^2}{\sum_i s_i n_i \mu_i^2}$, which reflects the competition between $n_h \mu_h^2$ and $n_e \mu_e^2$, it can be regarded as an effective weighted carrier concentration. This quantity can be estimated from the relation $\delta = 1/(R_0 e)$, as shown in Fig. 3(b). As temperature increases, δ initially rises gradually, followed by a sharp increase above $\sim$ 150 K, reaching a peak electron

concentration of -10.16×10^{22} cm^{-3} near 200 K, which is slightly larger than the carrier concentration in the Fe_3Sn_2 bulk crystal.[18,36] Beyond this point, δ exhibits a divergence and sign reversal above 20 K, at this critical temperature, δ attains a maximum positive value of 6.91×10^{22} cm^{-3}, indicating a transition from electron-dominated to hole-dominated transport. With further increases in temperature, δ gradually decreases toward 300 K. The divergence and polarity reversal of δ further confirm the scenario of Lifshitz transition within the multi-band system.

To further evaluate the AHE in Fe_3Sn_2 nanosheets, the anomalous Hall conductivity σ_{xy}^{A} is calculated using the relation $\sigma_{xy}^{A} = \rho_{yx}^{A} / \left(\rho_{xx}(0)^2 + \rho_{yx}^{A\,2}\right)$, where $\rho_{xx}(0)$ is the longitudinal resistivity in the absence of a magnetic field, and ρ_{xy}^{A} is the intercept extracted by fitting the high-field linear component of ρ_{xy}.[19,45] Figure 3(c) presents the temperature dependence of σ_{xy}^{A} over the range of 2–300 K. At $T = 2$ K, σ_{xy}^{A} reaches a maximum of 140 $\Omega^{-1} \cdot \text{cm}^{-1}$. As the temperature increases, σ_{xy}^{A} steadily decreases, reaching a minimum around 200 K. Beyond 200 K, σ_{xy}^{A} gradually rises, attaining higher values at 300 K. This temperature-dependent evolution of σ_{xy}^{A} suggests a potential crossover in the dominant mechanism driving the AHE across different temperature regimes.

Fe_3Sn_2 is a magnetic system with strong spin–orbit coupling, which provides the essential conditions for the AHE. In Fig. 3(d), σ_{xy}^{A} is plotted against σ_{xx}^{2} to examine the scaling relationship, aiming to elucidate the dominant AHE mechanism in Fe_3Sn_2 nanosheets. Considering both intrinsic and extrinsic contributions, σ_{xy}^{A} can be expressed as[46]

$$\sigma_{xy}^{A} = \alpha \sigma_{xx0}^{-1} \sigma_{xx}^{2} + \sigma_{xy}^{\text{int}}, \tag{5}$$

where α, σ_{xx0}, and σ_{xy}^{int} represent the skew-scattering coefficient, residual longitudinal conductivity, and intrinsic anomalous Hall conductivity, respectively. Fitting the data yields $\alpha = 0.00544$ and $\sigma_{xy}^{\text{int}} \approx 40.61$ $\Omega^{-1} \cdot \text{cm}^{-1}$ in the high-conductivity regime, and $\alpha = -0.07635$ and $\sigma_{xy}^{\text{int}} \approx 61.36$ $\Omega^{-1} \cdot \text{cm}^{-1}$ in the low-conductivity regime, which are comparable to values reported for bulk Fe_3Sn_2 (200 $\Omega^{-1} \cdot \text{cm}^{-1}$).[19] The negative α implies that the skew-scattering term opposes the intrinsic contribution, clarifying why the extracted σ_{xy}^{int} can exceed the measured total conductivity σ_{xy}^{A} in certain temperature ranges. Notably, σ_{xy}^{A} approaches σ_{xy}^{int} around 150–200 K, suggesting that the intrinsic Berry curvature contribution dominates in this regime. The sign change of α and the change in σ_{xy}^{int} around 200 K further supports the hypothesis of Fermi surface reconstruction across the Lifshitz phase transition. These findings are corroborated by additional measurements on a 30-nm-thick sample, as detailed in Fig. S1. While transport signatures — including the sign reversal of R_0 and the distinct evolution of the AHE — strongly indicate a Lifshitz transition at 200 K, direct spectroscopic confirmation through techniques such as angle-resolved photoemission spectroscopy (ARPES) would be invaluable and remains a goal for future investigation.

Finally, to demonstrate the reliability of our results, we compare the anomalous Hall conductivity σ_{xy}^{A} of Fe_3Sn_2 nanosheets with various reported ferromagnetic materials,[47–52] including bulk Fe_3Sn_2 crystals,[19] by plotting σ_{xy}^{A} versus σ_{xx} on a double-logarithmic scale, as shown in Fig. 4. According to the established unified theory for ferromagnets with dilute impurities, the scaling of σ_{xy}^{A} with σ_{xx} exhibits three distinct regimes: (i) in the superclean limit ($\sigma_{xx} > 10^6$ $\Omega^{-1} \cdot \text{cm}^{-1}$), $\sigma_{xy}^{A} \propto \sigma_{xx}$, dominated by extrinsic skew scattering;[53] (ii) in the moderately dirty regime (10^4 $\Omega^{-1} \cdot \text{cm}^{-1} < \sigma_{xx} < 10^6$ $\Omega^{-1} \cdot \text{cm}^{-1}$), σ_{xy}^{A} is nearly independent of σ_{xx}, characteristic of the intrinsic Berry curvature mechanism;[54] and (iii) in the bad-metal regime ($\sigma_{xx} < 10^4$ $\Omega^{-1} \cdot \text{cm}^{-1}$), σ_{xy}^{A} follows the relation $\sigma_{xy}^{A} \sim \sigma_{xx}^{1.6}$.[47] The observation of a quadratic scaling ($\sigma_{xy}^{A} \sim \sigma_{xx}^{2}$) in our CVD-grown Fe_3Sn_2 nanosheets, which resides in the intrinsic region, signals the coexistence of skew scattering and intrinsic Berry curvature mechanisms. Compared with bulk Fe_3Sn_2,[19] our nanosheets exhibit a clear Lifshitz transition and a lower onset temperature for spin reorientation, but also a reduced σ_{xy}^{A}, likely due to enhanced scattering or strain effects introduced during the CVD growth process. Nevertheless, these differences highlight the critical influence of reduced dimensionality and growth conditions on kagome metals, thereby offering a promising avenue for further tuning topological transport properties through nanoscale engineering and substrate coupling.

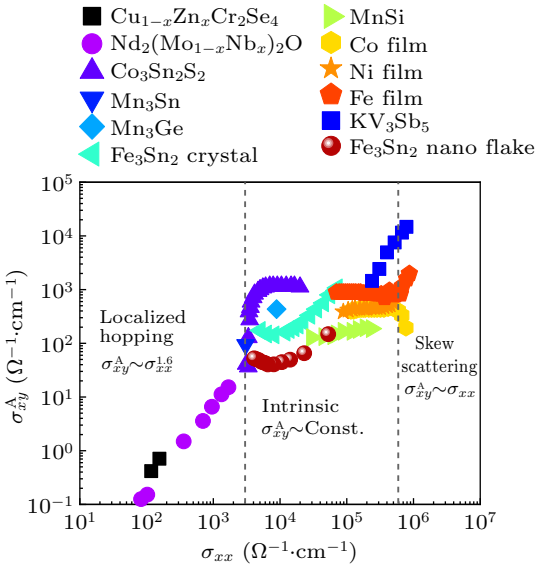


Fig. 4. Scaling plot of σ_{xy}^{A} vs. σ_{xx} for various materials, illustrating the different regimes of the AHE ranging from the side-jump mechanism through the intrinsic and skew scattering regimes.[19,47–52]

4. Conclusion and perspectives

In conclusion, we have systematically investigated the temperature-dependent transport properties in Fe_3Sn_2 nanosheets synthesized via chemical vapor deposition (CVD). A sharp reversal of the dominant transport contribution from electrons to holes near 200 K provides key evidence for a temperature-induced Lifshitz transition within the multi-band system. This interpretation is further supported by the distinct evolution of the anomalous Hall effect across the transition, where scaling analysis reveals a significant redistribution between intrinsic Berry curvature and skew scattering contributions across the transition. These observations are consistent with a Lifshitz transition in a multiband system and suggest a potential reconstruction of the Fermi surface topology. Our results highlight the sensitivity of anomalous Hall transport to temperature-driven band evolution in kagome magnets, and emphasize the potential of CVD-grown Fe_3Sn_2 nanosheets for scalable spintronic applications.

Acknowledgements

Project supported by the National Key Research and Development Program of China (Grant Nos. 2022YFA1403503, 2022YFA1602802, 2023YFA1607400, and 2024YFA1613200) and Beijing Natural Science Foundation (Grant No. JQ23022). This work is supported by the Synergetic Extreme Condition User Facility and the Innovation Program for Quantum Science and Technology (Grant No. 2021ZD0302600).

References

[1] Han T H, Helton J S, Chu S, Nocera D G, Rodriguez-Rivera J A, Broholm C and Lee Y S 2012 *Nature* **492** 406
[2] Liu Z, Bergholtz E J, Fan H and Läuchli A M 2012 *Phys. Rev. Lett.* **109** 186805
[3] Yin J X, Lian B and Hasan M Z 2022 *Nature* **612** 647
[4] Wang Q, Lei H, Qi Y and Felser C 2024 *Acc. Mater. Res.* **5** 786
[5] Nagaosa N, Sinova J, Onoda S, MacDonald A H and Ong N P 2010 *Rev. Mod. Phys.* **82** 1539
[6] Li X, Koo J, Zhu Z, Behnia K and Yan B 2023 *Nat. Commun.* **14** 1642
[7] Liu E, Sun Y, Kumar N, Muechler L, Sun A, Jiao L, Yang S-Y, Liu D, Liang A, Xu Q, Kroder J, Süß V, Borrmann H, Shekhar C, Wang Z, Xi C, Wang W, Schnelle W, Wirth S, Chen Y, Goennenwein S T B and Felser C 2018 *Nat. Phys.* **14** 1125
[8] Zhang Y, Wang C, Yu L, Liu G, Liang A, Huang J, Nie S, Sun X, Zhang Y, Shen B, Liu J, Weng H, Zhao L, Chen G, Jia X, Hu C, Ding Y, Zhao W, Gao Q, Li C, He S, Zhao L, Zhang F, Zhang S, Yang F, Wang Z, Peng Q, Dai X, Fang Z, Xu Z, Chen C and Zhou X J 2017 *Nat. Commun.* **8** 15512
[9] Wu L, Chi S, Zuo H, Xu G, Zhao L, Luo Y and Zhu Z 2023 *Npj Quantum Mater.* **8** 4
[10] Zheng Y, Chen W, Wan X and Xing D Y 2023 *Chin. Phys. Lett.* **40** 097301
[11] Li Y, Wu D, Shu Y, Liu B, Stuhr U, Deng G, Stampfl A P J, Zhao L, Zhou X, Li S, Pokhriyal A, Ghosh H, Hong W and Luo H 2025 *Chin. Phys. Lett.* **42** 067405
[12] Yuan M, Li Z, Zhang Q, Xia Z, Liu E and Liu Z 2023 *Appl. Phys. Lett.* **123** 182402
[13] Wang X, Pan D, Zeng Q, Chen X, Wang H, Zhao D, Xu Z, Yang Q, Deng J, Zhai T, Wu G, Liu E and Zhao J 2021 *Nanoscale* **13** 2601
[14] Wang X and Tan J 2023 *Appl. Phys. Lett.* **122** 051901
[15] Wang X and Tan J 2022 *Appl. Phys. Lett.* **121** 161903
[16] Fang S, Ye L, Ghimire M P, Kang M, Liu J, Han M, Fu L, Richter M, van den Brink J, Kaxiras E, Comin R and Checkelsky J G 2022 *Phys. Rev. B* **105** 035107
[17] Yin J X, Zhang S S, Li H, Jiang K, Chang G, Zhang B, Lian B, Xiang C, Belopolski I, Zheng H, Cochran T A, Xu S Y, Bian G, Liu K, Chang T R, Lin H, Lu Z Y, Wang Z, Jia S, Wang W and Hasan M Z 2018 *Nature* **562** 91
[18] Wang Q, Sun S, Zhang X, Pang F and Lei H 2016 *Phys. Rev. B* **94** 075135
[19] Ye L, Kang M, Liu J, von Cube F, Wicker C R, Suzuki T, Jozwiak C, Bostwick A, Rotenberg E, Bell D C, Fu L, Comin R and Checkelsky J G 2018 *Nature* **555** 638
[20] Wu P, Song J, Yu X, Wang Y, Xia K, Hong B, Zu L, Du Y, Vallobra P, Liu F, Torii S, Kamiyama T, Xiong Y and Zhao W 2021 *Appl. Phys. Lett.* **119** 082401
[21] Zhang D, Hou Z and Mi W 2022 *Appl. Phys. Lett.* **120** 232401
[22] Li H, Ding B, Chen J, Li Z, Hou Z, Liu E, Zhang H, Xi X, Wu G and Wang W 2019 *Appl. Phys. Lett.* **114** 192408
[23] Wang Q, Yin Q and Lei H 2020 *Chin. Phys. B* **29** 017101
[24] Hou Z, Ren W, Ding B, Xu G, Wang Y, Yang B, Zhang Q, Zhang Y, Liu E, Xu F, Wang W, Wu G, Zhang X, Shen B and Zhang Z 2017 *Adv. Mater.* **29** 1701144
[25] Tang J, Wu Y, Kong L, Wang W, Chen Y, Wang Y, Soh Y, Xiong Y, Tian M and Du H 2021 *Natl. Sci. Rev.* **8** nwaa200
[26] Du Q, Han M G, Liu Y, Ren W, Zhu Y and Petrovic C 2020 *Adv. Quantum Technol.* **3** 2000058
[27] Lin Z, Choi J H, Zhang Q, Qin W, Yi S, Wang P, Li L, Wang Y, Zhang H, Sun Z, Wei L, Zhang S, Guo T, Lu Q, Cho J H, Zeng C and Zhang Z 2018 *Phys. Rev. Lett.* **121** 096401
[28] Cheng S, Wang B, Lyalin I, Bagués N, Bishop A J, McComb D W and Kawakami R K 2022 *APL Mater.* **10** 061112
[29] Ren Z, Li H, Sharma S, Bhattarai D, Zhao H, Rachmilowitz B, Bahrami F, Tafti F, Fang S, Ghimire M P, Wang Z and Zeljkovic I 2022 *Npj Quantum Mater.* **7** 109
[30] Zhu M, Li Q, Guo K, Chen B, He K, Yi C, Lu P, Li X, Lu J, Li J, Wu R, Liu X, Liu Y, Liao L, Li B and Duan X 2024 *Nano Lett.* **24** 7483
[31] Wang Q, Sun S, Zhang X, Pang F and Lei H 2016 *Phys. Rev. B* **94** 075135
[32] Huang S, Zhu L, Zhao Y, Watanabe K, Taniguchi T, Xiao J, Wang L, Mei J, Huang H, Zhang F, Wang M, Fu D and Zhang R 2025 *Nat. Commun.* **16** 2866
[33] Zhang J, Ji W J, Xu J, Geng X Y, Zhou J, Gu Z B, Yao S H and Zhang S T 2017 *Sci. Adv.* **3** e1701473
[34] Salamon M B and Jaime M 2001 *Rev. Mod. Phys.* **73** 583
[35] Baibich M N, Broto J M, Fert A, Van Dau F N, Petroff F, Etienne P, Creuzet G, Friederich A and Chazelas J 1988 *Phys. Rev. Lett.* **61** 2472
[36] Wang L, Zhu J, Chen H, Wang H, Liu J, Huang Y X, Jiang B, Zhao J, Shi H, Tian G, Wang H, Yao Y, Yu D, Wang Z, Xiao C, Yang S A and Wu X 2024 *Phys. Rev. Lett.* **132** 106601
[37] McKenzie R H 1998 *Phys. Rev. B* **57** 11854
[38] Li Q, Wang B, Tang N, Li C, Yi E, Shen B, Guo D, Zhong D and Wang H 2023 *Chin. Phys. Lett.* **40** 067101
[39] Lin Z 2018 *Phys. Rev. Lett.* **121** 020403
[40] Tanaka H, Fujisawa Y, Kuroda K, Noguchi R, Sakuragi S, Bareille C, Smith B, Cacho C, Jung S W, Muro T, Okada Y and Kondo T 2020 *Phys. Rev. B* **101** 161114
[41] Ekahana S A, Soh Y, Tamai A, Gosálbez-Martínez D, Yao M, Hunter A, Fan W, Wang Y, Li J, Kleibert A, Vaz C A F, Ma J, Lee H, Xiong Y, Yazyev O V, Baumberger F, Shi M and Aeppli G 2024 *Nature* **627** 67
[42] Chen F C, Fei Y, Li S J, Wang Q, Luo X, Yan J, Lu W J, Tong P, Song W H, Zhu X B, Zhang L, Zhou H B, Zheng F W, Zhang P, Lichtenstein A L, Katsnelson M I, Yin Y, Hao N and Sun Y P 2020 *Phys. Rev. Lett.* **124** 236601
[43] Lozano P M, Cardoso G, Aryal N, Nevola D, Gu G, Tsvelik A, Yin W and Li Q 2022 *Phys. Rev. B* **106** L081124

[44] Wu Y, Jo N H, Ochi M, Huang L, Mou D, Bud'ko S L, Canfield P C, Trivedi N, Arita R and Kaminski A 2015 *Phys. Rev. Lett.* **115** 166602
[45] Mai D, Zhao J, Zhong C, Ye C, Zhao H, Zhang Y, Li J, Wang H, Sun X, Dai R, Wang Z, Rahman A, Wang X and Zhang Z 2025 *Appl. Mater. Today* **45** 102794
[46] Tian Y, Ye L and Jin X 2009 *Phys. Rev. Lett.* **103** 087206
[47] Iguchi S, Hanasaki N and Tokura Y 2007 *Phys. Rev. Lett.* **99** 077202
[48] Nayak A K, Fischer J E, Sun Y, Yan B, Karel J, Komarek A C, Shekhar C, Kumar N, Schnelle W, Kübler J, Felser C and Parkin S S P 2016 *Sci. Adv.* **2** e1501870
[49] Nakatsuji S, Kiyohara N and Higo T 2015 *Nature* **527** 212
[50] Liu E, Sun Y, Kumar N, Muechler L, Sun A, Jiao L, Yang S-Y, Liu D, Liang A, Xu Q, Kroder J, Süß V, Borrmann H, Shekhar C, Wang Z, Xi C, Wang W, Schnelle W, Wirth S, Chen Y, Goennenwein S T B and Felser C 2018 *Nat. Phys.* **14** 1125
[51] Yang S Y, Wang Y, Ortiz B R, Liu D, Gayles J, Derunova E, Gonzalez-Hernandez R, Šmejkal L, Chen Y, Parkin S S P, Wilson S D, Toberer E S, McQueen T and Ali M N 2020 *Sci. Adv.* **6** eabb6003
[52] Miyasato T, Abe N, Fujii T, Asamitsu A, Onoda S, Onose Y, Nagaosa N and Tokura Y 2007 *Phys. Rev. Lett.* **99** 086602
[53] Smit J 1955 *Physica* **21** 877
[54] Karplus R and Luttinger J M 1954 *Phys. Rev.* **95** 1154